

# An Alternative Pressure-dependent Friction Boundary Condition for Modeling Self-reacting Friction Stir Welding

CHENYU ZHAO

The Ohio State University <https://orcid.org/0000-0002-1837-9149>

Xun Liu ([✉ liu.7054@osu.edu](mailto:liu.7054@osu.edu))

Department of Material Science and Engineering, The Ohio State University, Columbus 43221, Ohio, USA

---

## Research Article

**Keywords:** self-reacting friction stir welding, wear theory, shear layer, boundary condition, CFD model

**Posted Date:** March 29th, 2021

**DOI:** <https://doi.org/10.21203/rs.3.rs-354150/v1>

**License:**  This work is licensed under a Creative Commons Attribution 4.0 International License.  
[Read Full License](#)

---

**Version of Record:** A version of this preprint was published at The International Journal of Advanced Manufacturing Technology on August 10th, 2021. See the published version at <https://doi.org/10.1007/s00170-021-07589-z>.

# An alternative pressure-dependent friction boundary condition for modeling Self-reacting Friction Stir Welding

Chenyu Zhao, Xun Liu\*

Department of Material Science and Engineering, The Ohio State University, Columbus 43221, Ohio,  
USA

Corresponding author: liu.7054@osu.edu

## Abstract

A pressure-dependent friction boundary condition is developed based on wear theory for modeling self-reacting friction stir welding using computational fluid dynamics approach. The importance of shear layer in weld formation is emphasized. Effects of welding speed on the weld cross section geometry can be robustly captured with this newly developed boundary condition. Computational results showed at higher welding speed, the distance between the TMAZ boundary and the pin periphery at the advancing side is reduced, which corresponds to the experimental observations. This tendency could serve as a numerical criterion to predict void defect formation.

Keywords: self-reacting friction stir welding, wear theory, shear layer, boundary condition, CFD model

## 1. Introduction

Self-reacting friction stir welding (SRFSW) is an advanced variant of friction stir welding (FSW), which utilizes a double-sided tool and shows several superiorities. The additional root shoulder can effectively avoid root penetration defects in conventional FSW welds. Meanwhile, axial force between the crown and root shoulder surface is balanced, which results in a trivial net axial force and enables in-space FSW without requirement of heavy manufacturing equipment. SRFSW can be divided into two categories based on tool designs. First is the fixed gap bobbin tool [1], where the distance between crown and root shoulder is constant. The second is the adaptive tool [2], where the distance between crown and root shoulder can be dynamically controlled according to the force acting between the two shoulders. One typical application of SRFSW is manufacturing large-scale cryogenic fuel tanks in space vehicles.

Recognizing the importance of understanding the weld formation mechanism during FSW/SRFSW, various researches have been taken to investigate the experimentally observed shear layer [3–5] formed in the process. As a result of the interactions between the tool and the workpiece, localized shear develops in the tool vicinity and forms a narrow region of intense plastic deformation, i.e., shear layer, which is also referred to as shear band [6,7]. Shear layer formation in shear dominated processes is generally believed to be first observed by Tresca [8]. To understand this deformation localization mechanism, Batra and Wei [6] analyzed the initiation and development of shear layer using one-dimensional (1D) transient thermo-elasto-viscoplastic formulation, with prescribed tangential velocity and constant heat flux as boundary conditions. They found that the shear band initiation time closely depends upon the prescribed heat flux. Pei and Dong [9] incorporated this 1D shear localization model into FSW process modeling, with different boundary and initial conditions. In their following study [10], they used Zener-Hollomon material constitutive model instead of Johnson-Cook model, which was previously used in [6,9]. They calculated the width, formation time and propagation speed of shear layer. The propagation speed serves as an estimation of the possible allowed maximum welding speed for a given material with certain welding parameters.

Compared with shear localization model which only provides information surrounding the tool, thermo-mechanical computational fluid dynamics (CFD) models are capable of predicting the entire weld cross section morphology [11,12], visualizing flow field [12–14] and obtaining weld thermal history [12,13,15,16]. Due to the complexities of the sticking/sliding transition behavior between tool and workpiece, different assumptions and simplifications have been made at tool/workpiece (T/W) boundary. One is velocity boundary condition, where a prescribed velocity is assigned at T/W interface. The value can be equal to the tool velocity [13,17] representing a full sticking condition, or a fraction of tool velocity representing a partially sticking condition. The fraction is either a constant [18] or a preassigned variable as an (empirical) function of the radial distance [19–22]. The other group of T/W boundary condition is based on friction stress [16,23], and the velocity of interfacial material is solved implicitly. Zhao and Liu [12] evaluated the credibility of velocity and shear stress boundary condition based on the calculated weld cross-sectional morphology. According to their work, the shear stress boundary condition represents T/W sliding in Coulomb friction and subsurface interfacial sliding in Tresca friction, whereas the velocity boundary condition represents an averaging estimated sticking/sliding transition state of the shear layer, which is more appropriate to model the actual T/W contact behavior. However, owing to the lack of fundamental understanding of the T/W friction behavior and challenges of direct experimental observations, an explainable velocity boundary condition which combines pressure distribution that can be implemented under various welding parameters and produce robust predictions in CFD-based SRFSW/FSW process models is still missing.

The focus of this study is on developing a new pressure-dependent velocity boundary condition based on wear theory, which provides a new and explainable perspective in understanding the physics of sliding/sticking condition and shear layer formation mechanism during FSW/SRFSW CFD modeling. The corresponding weld cross-sectional morphology is predicted based on plastic strain distribution and validated with experimental macrographs at different welding speeds. The rationale behind pure velocity and pressure-dependent velocity boundary condition will be compared and evaluated.

## 2. Modeling Approaches

### 2.1 Governing equations

In CFD-based FSW/SRFSW modeling, solid state metals are treated as non-Newtonian fluids with high viscosities. For incompressible single-phase fluid, governing equations of the mass, momentum and energy conservation equations are as follows,

$$\nabla \cdot \vec{v} = 0 \quad (1)$$

$$\rho \left( \frac{\partial \vec{v}}{\partial t} + \vec{v} \cdot \nabla \vec{v} \right) = -\nabla p + \nabla \cdot (\mu \cdot \nabla \vec{v}) \quad (2)$$

$$\rho \left( \frac{\partial (C_p T)}{\partial t} + \nabla \cdot (\vec{v} C_p T) \right) = \nabla \cdot (k \nabla T) + S_v \quad (3)$$

where  $\vec{v}$  is the velocity vector,  $\rho$  the density,  $t$  the time,  $p$  the pressure,  $C_p$  the specific heat capacity,  $k$  the thermal conductivity,  $S_v$  the spatial heat source term from plastic deformation.  $\mu$  is the effective viscosity. The viscoplastic material mechanical behavior is described by the Sellars-McTegart constitutive model [24]:

$$\dot{\epsilon}_e = A \left[ \sinh(\alpha \sigma_e) \right]^n \exp\left(-\frac{Q}{RT}\right) \quad (4)$$

where  $\sigma_e$  is flow stress,  $Q$  the deformation activation energy,  $R$  the gas constant,  $T$  the absolute temperature;  $A$ ,  $\alpha$  and  $n$  are material constants. Effective strain rate is given by [17,25]:

$$\dot{\epsilon}_e = \left( \frac{2}{3} \mathbf{D} \cdot \mathbf{D} \right)^{\frac{1}{2}} \quad (5)$$

where  $\mathbf{D}$  is the strain rate tensor:

$$\mathbf{D} = \frac{1}{2} \left( \nabla \mathbf{v} + (\nabla \mathbf{v})^T \right) \quad (6)$$

In incompressible single-phase flow,  $\frac{\partial v_i}{\partial x_i} = 0$ . Effective viscosity  $\mu$  could be calculated from effective stress  $\sigma_e$  and effective strain rate  $\dot{\epsilon}_e$  as [17,23,26]

$$\mu = \frac{\sigma_e}{3 \dot{\epsilon}_e} \quad (7)$$

Flow stress in Eq. (4) could also be rewritten as [27]

$$\sigma_e = \frac{1}{\alpha} \ln \left\{ \left( \frac{Z}{A} \right)^{\frac{1}{n}} + \left[ \left( \frac{Z}{A} \right)^{\frac{2}{n}} + 1 \right]^{\frac{1}{2}} \right\} \quad (8)$$

where  $Z$  is the Zener-Hollomon parameter, which represents the temperature compensated effective strain rate and is expressed as

$$Z = \dot{\epsilon}_e \exp\left(\frac{Q}{RT}\right) \quad (9)$$

Material parameters in AA6061-T6 constitutive models are listed in Table 1 according to tensile experimental data in [16]. Table 1 also provides the thermo-physical properties of AA6061-T6 implemented in the model. An artificial term is added in Eq. (8) to enforce flow stress decreases to zero as temperature approaches solidus of AA6061-T6.

Table 1 Constitutive parameters and thermo-physical properties of AA6061-T6 implemented in this study [16]

Parameters	Value
$\alpha$	33.9 MPa
$A$	$8.91 \times 10^{13} \text{ s}^{-1}$
$n$	5.06
$Q$	$(234 - 0.0244 \times T) \text{ kJ/mol}$
$R$	8.314 J/mol K
$\rho$	2700 kg/m <sup>3</sup>
$C_p$	896 J/kg K
$k$	167 W/m K

## 2.2 Boundary conditions

In this study, two mechanical T/W boundary conditions are investigated. The first one is the constant pure velocity boundary condition, and the second is the pressure-dependent velocity boundary condition, which is derived from the modified Archard's wear equation.

In the constant velocity boundary, the material velocity at interface is directly assigned as a fraction of tool velocity as,

$$v_b = \delta v_{tool}^I \quad (10)$$

where  $\delta$  represents the degree of sticking and an averaging effect of the shear layer [12]. As  $\delta$  increases, the predicted width of deformation zone increases accordingly since higher boundary velocity intensifies the material movement in the pin vicinity. By adjusting modeling results to match with the experimental weld cross-section morphology in [28], the value of  $\delta$  is determined as 0.013.

The second T/W boundary condition is based on wear theory. Conventionally, wear models are applied in FSW to predict FSW tool wear [29]. In contrary, this study adopts an opposite perspective and considers the FSW/SRFSW process as the wear of the workpiece. In other words, to capture the shear layer, the wear model is implemented on workpiece instead of the tool. This assumption is reasonable since the tool always has higher hardness than the workpiece material. As the workpiece materials are worn by the friction action of the tool, the worn metal forms a rotating shear layer surrounding the tool and deposited backward in the weld. Figure 2 shows the experimental observations of shear layer during FSW. The importance of this shear layer formation to achieve a defect-free welds has also been discussed in [12].

Wear damage of the workpiece can be described by Archard's Equation [30]:

$$V = kWS \quad (11)$$

where  $V$  is the total wear volume;  $k$  is the dimensional Archard wear coefficient, which depends on the material and surface cleanliness;  $W$  is the applied load;  $S$  is the sliding distance between the tool and the workpiece. The thickness of shear layer can be represented by the wear depth. Therefore, the modified Archard's Equation [29] is adopted as:

$$h = kptv_{slip} \quad (12)$$

where  $h$  is the wear depth,  $p$  the contact pressure,  $t$  the time,  $v_{slip}$  the relative velocity between the tool and the workpiece.

According to Eq. (11) or Eq. (12), in Archard's wear model, the worn material/shear layer is continuously generated and has the same velocity as the tool, which represents the full sticking scenario. However, during FSW/SRFSW, it is known that the T/W interface is subject to a complex sticking/sliding transition state, where the sticking and sliding condition varies along tool surface [12]. As shown in Figure 1, in the scenario of full sticking, the velocity of the material at T/W interface equals the tool velocity, and the shear layer continuously forms. When pure sliding happens, the wear of workpiece does not occur, and the generation of the shear layer stops, and the velocity of the formed shear layer equals to zero. From the modeling perspective, the velocity of the shear layer is supposed to be estimated and applied as the T/W workpiece boundary condition. Under the same rotation speed of the tool, the sliding distance between the shear layer and the remaining material of the workpiece can be written as,

$$S'_{\text{slip}} = \beta S_{\text{tool}} - S_{\text{mat}}, \quad (13)$$

and the relative velocity between the shear layer and the remaining material can be obtained as,

$$v'_{\text{slip}} = \beta v_{\text{tool}} - v_{\text{mat}}, \quad (14)$$

where  $\beta(p,t)$  defined as wear fraction coefficient, which is a function of pressure and time, represents the fraction of wear happened along the tool traveled distance.  $\beta v_{\text{tool}}$  represents the velocity of the shear layer  $v_{\text{shear layer}}$ .  $S_{\text{tool}}$  is the distance the tool moves;  $S_{\text{mat}}$  is the distance remaining material moves;  $v_{\text{tool}}$  is the tool velocity;  $v_{\text{mat}}$  is the remaining material velocity. Different from a constant value of  $\delta$  in Eq. (10),  $\beta(p,t)$  is dependent on the wear condition, which should be a function of pressure and time based on Archard's wear model.  $\beta(p,t)$  is an advanced version of  $\delta$  and provides a more accurate estimation of the equivalent shear layer velocity in sticking/sliding transition state.  $\beta(p,t)$  and  $\delta$  have the same magnitude.

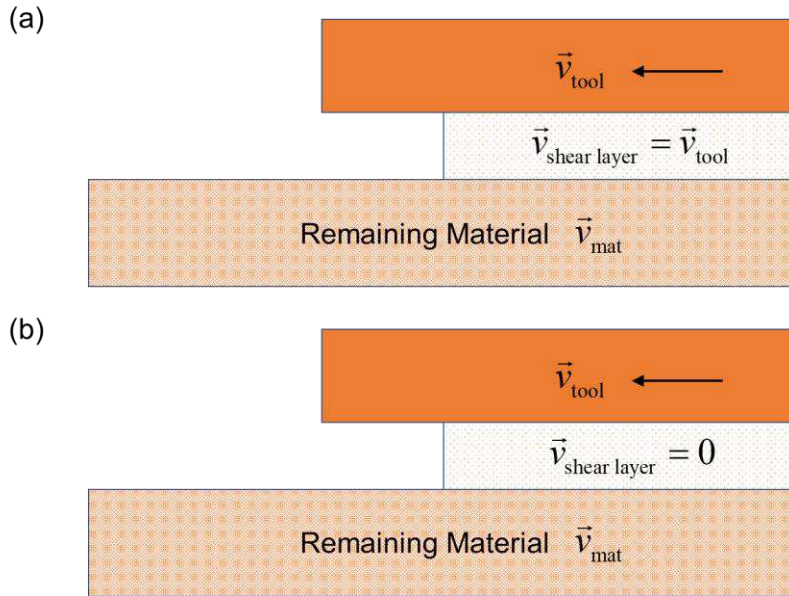


Figure 1 Illustration of sticking/sliding transition state at T/W interface: (a) Full sticking; (b) Pure sliding.

Since the relative velocity is time-dependent, furthermore, the SRFSW is treated as quasi-steady state in process modeling, the wear depth can be calculated as,

$$h = kp \int_{t_1}^{t_2} v'_{\text{slip}} dt = kp (\bar{\beta} v_{\text{tool}} - \bar{v}_{\text{mat}}) \Delta t \quad (15)$$

Where  $t_1$  is the moment when shear layer starts to form and  $t_2$  is the moment when the shear layer detaches from the tool.  $\bar{\beta}(p)$  is the time-averaged wear fraction coefficient of  $\beta(p,t)$ , which is a function of pressure;  $\bar{v}_{\text{mat}}$  is the averaged remaining material velocity;  $\Delta t = t_2 - t_1$  is the total existing time of each shear layer.  $\bar{v}_{\text{mat}}$  and  $\Delta t$  are constants under the same welding condition.

During FSW, a newly formed shear layer is established and circulates around the pin for a short distance to the trailing side until it deposits [4]. This is defined as one wear cycle, which

happens every tool revolution. When the welding speed is constant, the average thickness of the worn material during each wear cycle remains constant to form a weld. This agrees well with experimental observations of the uniform thickness of shear layer during each wear cycle [4,5,31] as shown in Figure 2.

When the welding speed varies within a reasonable range, based on experimental observations from literature [28,32], void defects always occur at advancing side due to the lack of deposition, i.e., the shear layer could not be transported to a sufficient distance into the advancing side, rather than occur between shear layers. This indicates the amount of shear layer generated is adequate under different welding speeds without leaving lack of fills in between successive layers. Therefore, according to the geometrical restriction, at the same rotation speed, the thickness of the shear layer could be assumed to be proportional to the welding speed [4,33].

Therefore, according to Eq. (15), the pressure-dependent velocity boundary condition can be formulated as,

$$v_{shearlayer} = \bar{\beta} v_{tool} = \bar{v}_{mat} + \frac{h}{\Delta t k p} = \alpha \left( 1 + \frac{\gamma v_{welding}}{p} \right) \quad (16)$$

where  $\alpha$  and  $\gamma$  are constants,  $v_{welding}$  the welding speed. Eq. (16) only holds when  $p$  is larger than a threshold value. Formation of shear layer would not occur when  $p$  is low, and the boundary velocity would decrease to zero accordingly. By calibrating the modeling results with the experimental weld cross-section morphology, the values of  $\alpha$  and  $\gamma$  are determined as 0.0095 and 4.5E5 when the unit of  $v_{welding}$  is mm/min. It should be noted that continuity is required in the CFD computational domain. Accordingly, both pure velocity boundary condition and pressure-dependent velocity boundary condition represent an estimation of the equivalent shear layer velocity to capture the effects of the shear layer on the remaining material. The shear layer itself is not explicitly modeled.

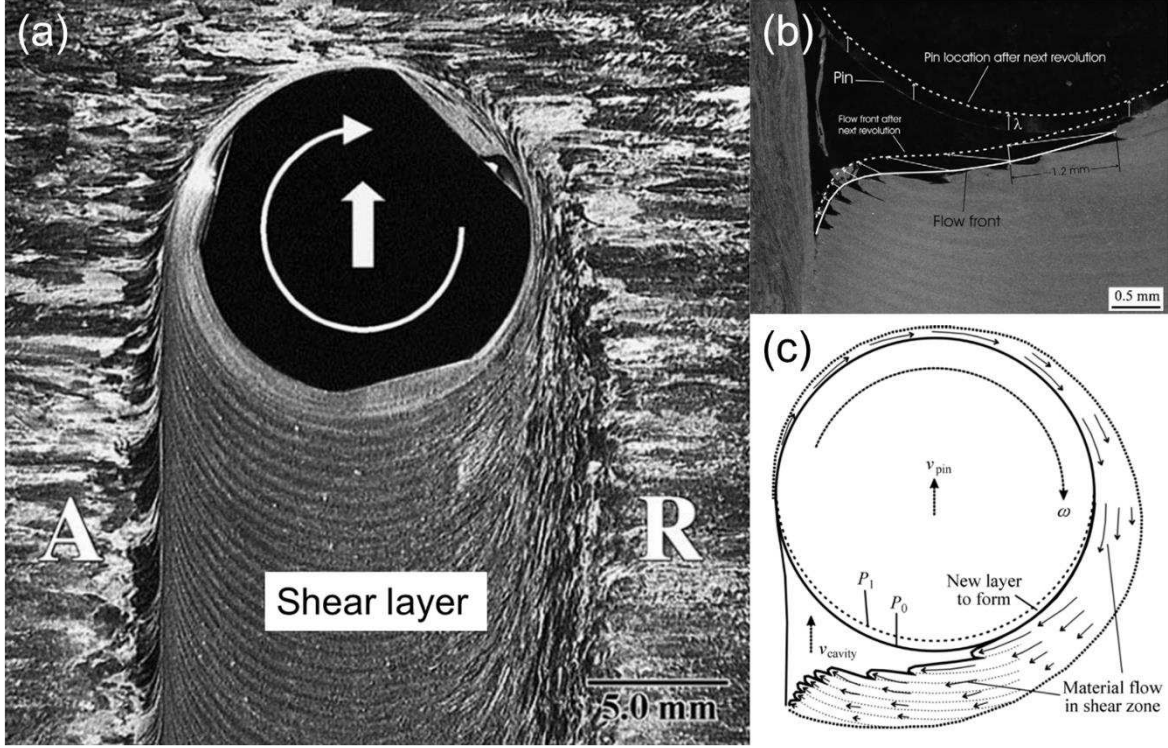


Figure 2 (a) Top view of shear layer in FSW [31], (b) shear layer behind the pin in FSW [5], (c) schematic illustration of shear layer around the pin [4]

From thermal perspective, frictional heat generation rate at T/W interface is calculated as

$$q_{tool} = \zeta \tau_b |v_{rel}|^r \quad (7)$$

where  $\zeta$  is the heat partition coefficient, which represents the fraction of heat absorbed by the workpiece compared with total amount of generated heat.  $\zeta$  can be calculated by [20]

$$\zeta = \frac{\sqrt{(k\rho C_p)_{workpiece}}}{\sqrt{(k\rho C_p)_{workpiece}} + \sqrt{(k\rho C_p)_{tool}}} \quad (8)$$

The heat partition coefficient at the bottom shoulder is 0.9. A slightly smaller heat partition coefficient of 0.8 is selected at the top shoulder since it is clamped into the entire machine, which acts as a large heat sink leading to higher amount of heat dissipation.

On the remaining surfaces of workpiece, convective heat transfer boundary conditions are adopted. The convection heat transfer coefficient and environment temperature are set as 20W/m<sup>2</sup>K and 300K, respectively.

### 2.3 Numerical Model Geometry and Particle Tracing Methodology

A schematic illustration of the computational domain is provided in Figure 3. The SRFSW tool is hollowed out from the workpiece. Dimensions and geometry of the tool and the workpiece are consistent with the experimental configurations described in [28]. The calculation domain contains an inlet and an outlet surface indicating the direction of welding speed. Thickness of the workpiece is 4mm. The diameters of the non-threaded pin, top and bottom shoulder are 8mm, 18mm and 16mm, respectively. Plunge depth of both top and bottom shoulder is 0.1mm.

Interactions between tool and workpiece are incorporated with corresponding thermo-mechanical boundary condition models described above, which are encoded with user defined functions (UDF) and implemented into the FLUENT program. In this study, four cases are calculated and compared, as summarized in Table 2.

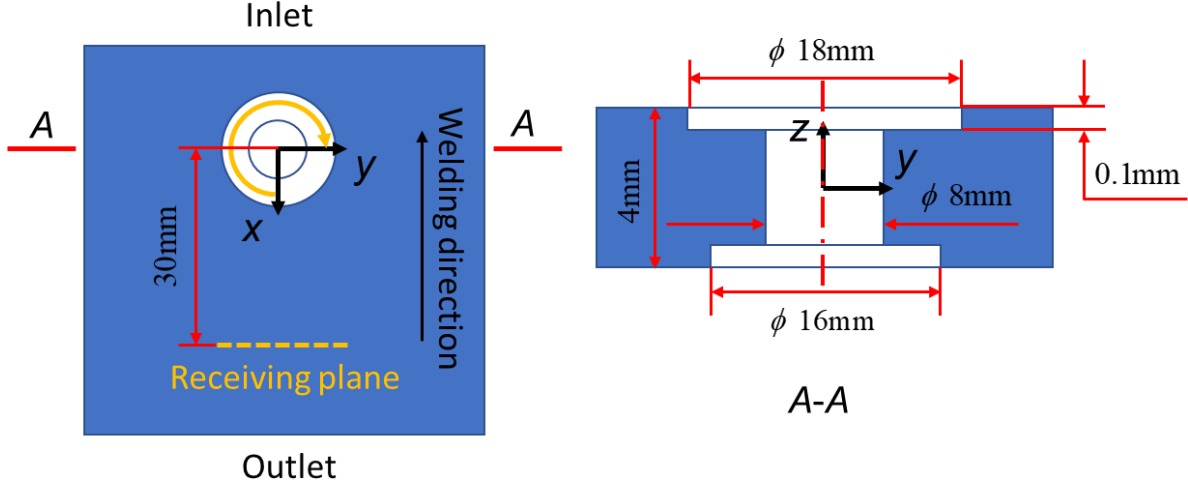


Figure 3 Illustration of model geometry

Particle tracing methodology is adopted according to Ref. [12] to determine the strain distribution on the weld section behind the pin, after the simulation entered the quasi-steady state. A virtual receiving plane of  $20\text{mm} \times 3.8\text{mm}$  is placed at 30mm behind the tool center, where the stirring effects of pin on material flow diminished. A total number of 1600 of particles are traced. The strain can be calculated by integrating the effective strain rate over time. By combining the relationship between time and velocity, the strain at each point on the receiving plane can be integrated along path lines as

$$\varepsilon = \int_{t_1}^{t_2} \dot{\varepsilon} dt = \int_{l_1}^{l_2} \frac{\dot{\varepsilon}}{v} dl \quad (9)$$

Where  $v$  is the local velocity magnitude.

Table 2 Four cases settings

	Welding speed	Boundary condition	Rotation speed
Case 1	100mm/min	Pure velocity B.C.	600rpm
Case 2	100mm/min	Pressure-dependent velocity B.C.	600rpm
Case 3	150mm/min	Pressure-dependent velocity B.C.	600rpm
Case 4	250mm/min	Pressure-dependent velocity B.C.	600rpm

### 3. Results and Discussion

#### 3.1 Strain Distribution and Weld Cross-sectional Morphology Prediction

Figure 4 to Figure 7 show the strain distribution on the weld cross-section at 30mm behind the tool center of the four simulated cases. The SRFSW tool profile are marked out with red dotted lines on the calculated iso-strain contour maps and experimental weld macrographs. Boundary of deformation zone, including both stirring zone (SZ) and thermo-mechanically affected zone

(TMAZ) can be sketched with iso-strain contours since these two zones were subject to mechanical deformation during the welding process. At the advancing side, the iso-strain contours are denser than the retreating side, indicating higher spatial gradient of strain. This is consistent with the general SRFSW weld macrograph observations, where the boundary between TMAZ and HAZ is more definable in the advancing side whereas gradual transition occurs at the retreating side. Comparing Figure 4 and Figure 5, under the same welding speed of 100mm/min, pure velocity boundary condition (case 1) and pressure-dependent velocity boundary condition (case 2) predict similar iso-strain contours at the advancing side, both of which are in line with the experimentally observed TMAZ boundary. The distance between the pin periphery and the iso-strain contour at the neck of the hourglass morphology is also in agreement with the weld macrograph. In contrary, the morphology in the retreating side is hardly captured with the pure velocity boundary, where the high strain contours deviate significantly in the crown shoulder region, as shown in the left side of Figure 4. This is greatly improved with the newly developed pressure-dependent boundary condition, as shown in Figure 5.

As welding speed increases from 100mm/min to 250mm/min, based on the pressure-dependent velocity boundary, the predicted TMAZ boundary in the advancing side moves towards the pin center, as shown from Figure 5 to Figure 7. This trend is in consistent with the experimental observations. At the highest welding speed of 250mm/min, the TMAZ boundary almost overlaps with the pin periphery in both the computational results and the experimental weld macrographs, as shown in Figure 7. This high welding speed parameter actually leads to the formation of void defect, which is located at the pin periphery in the advancing side as in Figure 7 (c). Generally, in the SRFSW process, the welding parameters that lead to void defects formed at this location would also result in the very close distance between the TMAZ boundary and the pin periphery in the advancing side, as shown in Figure 8. Accordingly, the relative position of the predicted TMAZ boundary to the pin periphery in the advancing side could serve as an effective criterion for void defect prediction.

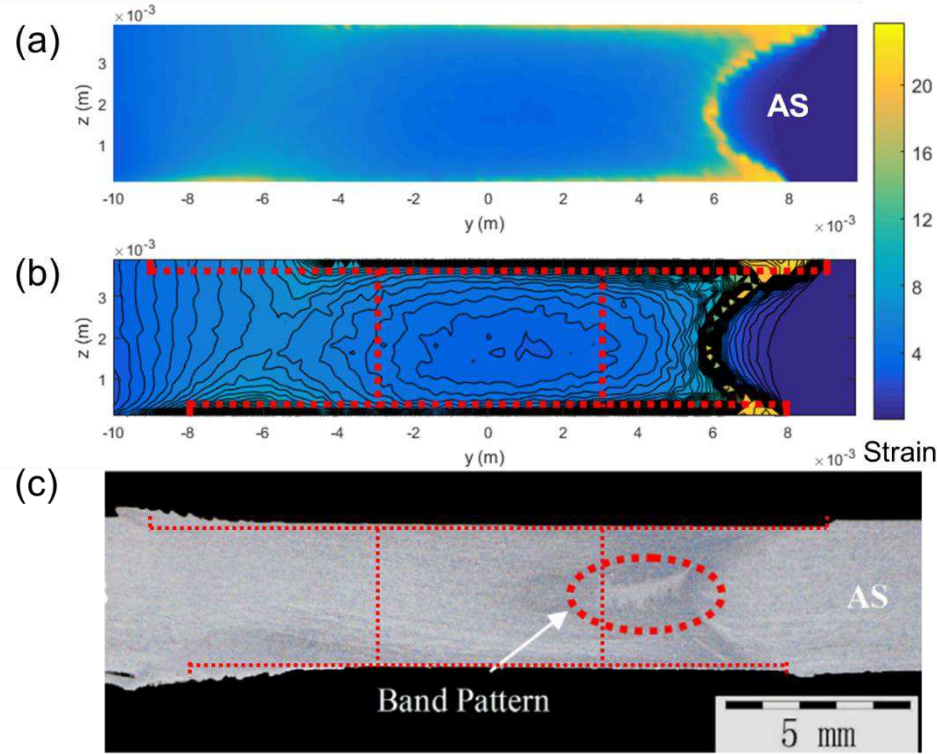


Figure 4 (a) Cloud map of predicted strain distribution at 30mm behind tool center in case 1, (b) Iso-strain contour map at 30mm behind tool center in case 1, (c) Cross section of SRFSW weld under welding speed of 100mm/min from reference [28]

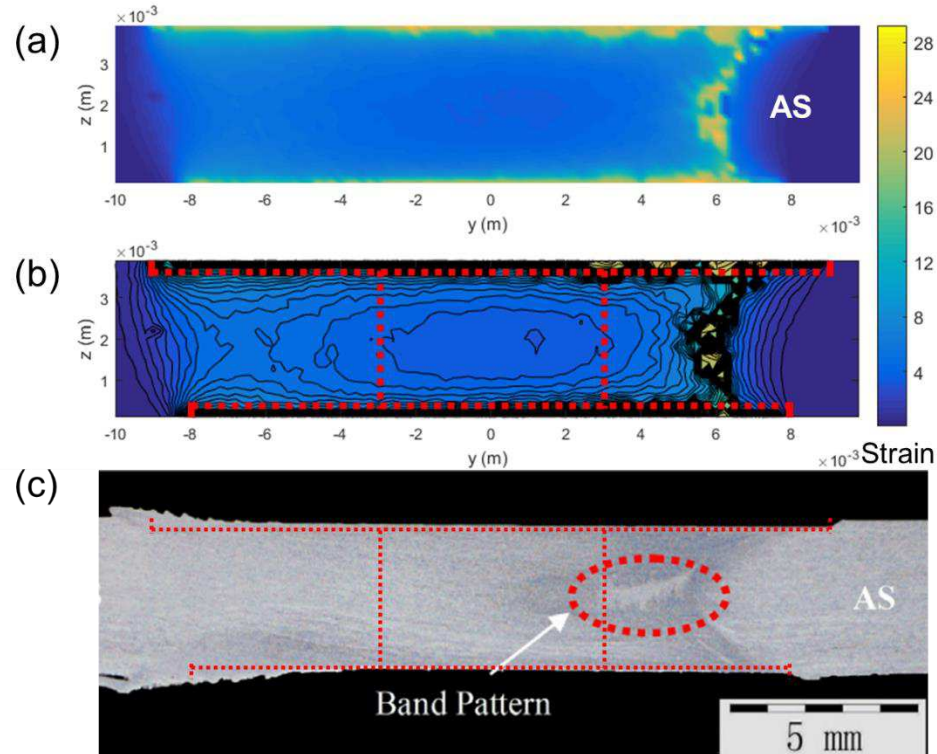


Figure 5 (a) Cloud map of predicted strain distribution at 30mm behind tool center in case 2, (b) Iso-strain contour map at 30mm behind tool center in case 1, (c) Cross section of SRFSW weld under welding speed of 100mm/min from reference [28]

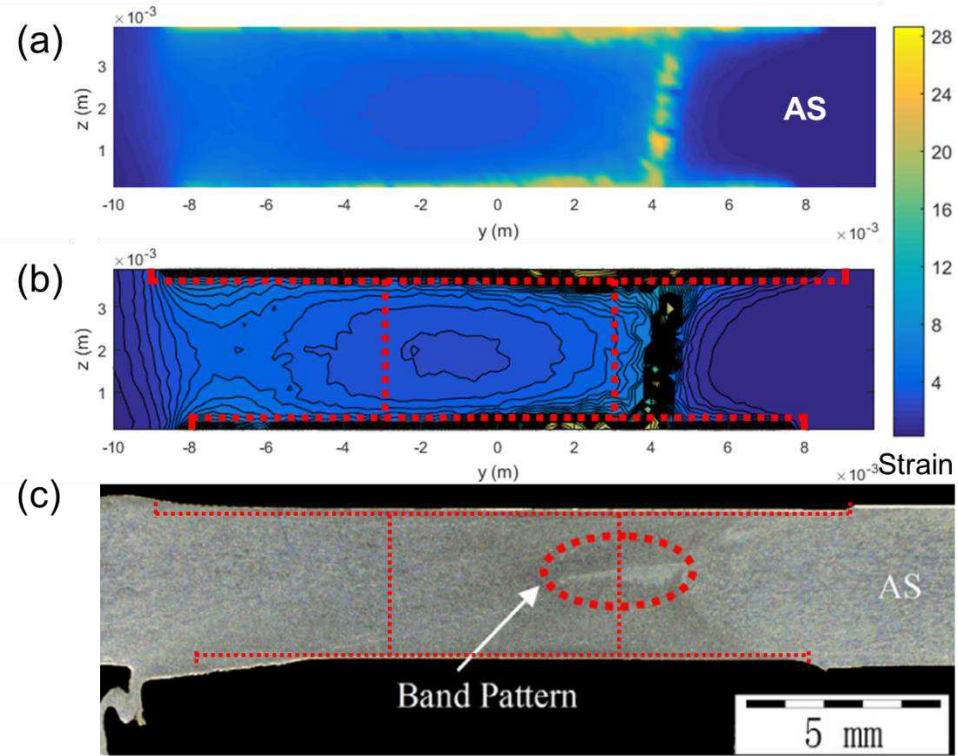


Figure 6 (a) Cloud map of predicted strain distribution at 30mm behind tool center in case 3, (b) Iso-strain contour map at 30mm behind tool center in case 1, (c) Cross section of SRFSW weld under welding speed of 150mm/min from reference [28]

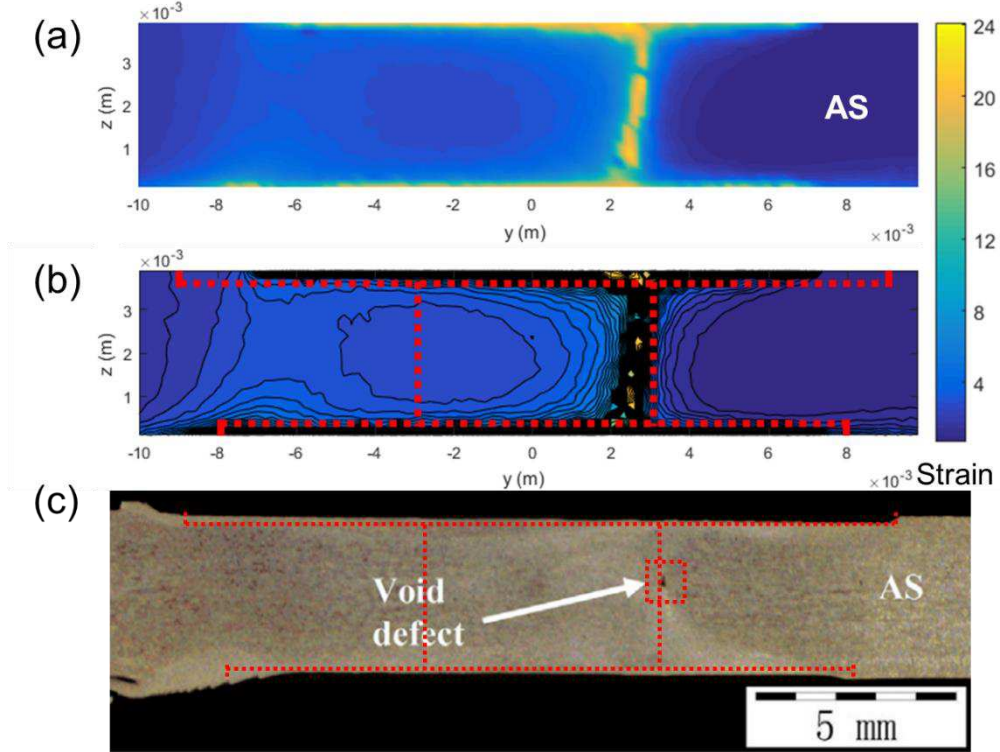


Figure 7 (a) Cloud map of predicted strain distribution at 30mm behind tool center in case 4, (b) Iso-strain contour map at 30mm behind tool center in case 1, (c) Cross section of SRFSW weld under welding speed of 250mm/min from reference [28]

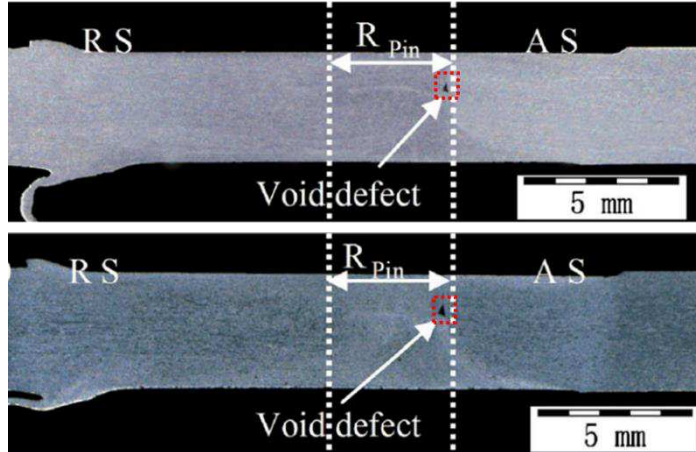


Figure 8 Cross section of SRFSW welds of AA6061-T6 from reference [32]

### 3.2 Flow field and pressure distribution

Material flow field of the four cases are provided in Figure 9. The path line distributions are overall similar. Incoming materials are mainly plasticized at retreating side and some fractions are deposited backward at advancing side. The red arrow indicates the position where the materials start to deposit. As the welding speed increases, the deposition position moves away from the shoulder edge in the advancing side towards the pin center, which means less amount of material is transported to a sufficient distance to fill up the advancing side. This tendency matches well with the weld cross section morphology from Figure 5 to Figure 7. Since less amount of material

is stirred into the advancing side, the deformation zone size is narrowed and leads to a closer distance between the pin periphery and the TMAZ boundary. When the amount of material filled into advancing side drops below a certain degree, void defect is formed as shown in Figure 9 (d) and Figure 7.

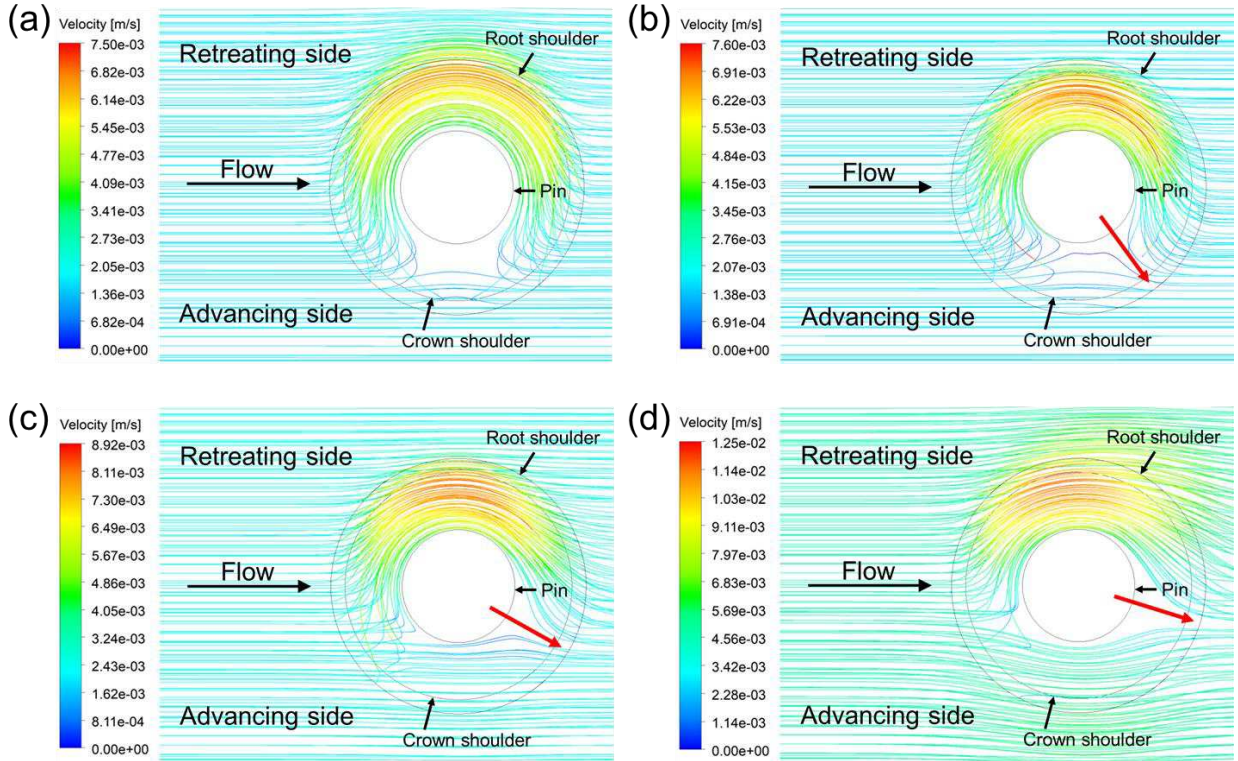


Figure 9 Material flow field in (a) Case1: 100mm/min, pure velocity boundary, (b) Case2: 100mm/min, pressure-dependent velocity boundary, (c) Case3: 150mm/min, pressure-dependent velocity boundary, (d) Case4: 250mm/min, pressure-dependent velocity boundary

The velocity distribution on the mid-pin depth plane is shown in Figure 10. As the welding speed increases from Figure 10 (b) to Figure 10 (d), overall the magnitude of material velocity increases. The red arrow in these figures points towards the low velocity region and its rotating direction agrees with that of flow field distribution (red arrow in Figure 9) as the welding speed increases. Under pure velocity boundary condition in Figure 10 (a), the magnitude of velocity is distributed relatively symmetric in front and behind the pin. With the pressure dependent velocity boundary condition, the shape of velocity magnitude field is distorted and points towards the position where materials start to deposit at advancing side, as discussed in Figure 9. Comparing Figure 10 (a) and Figure 10 (b), under the same welding speed of 100mm/min, the maximum velocity under both the pure velocity and the pressure-dependent velocity boundary condition is about the same.

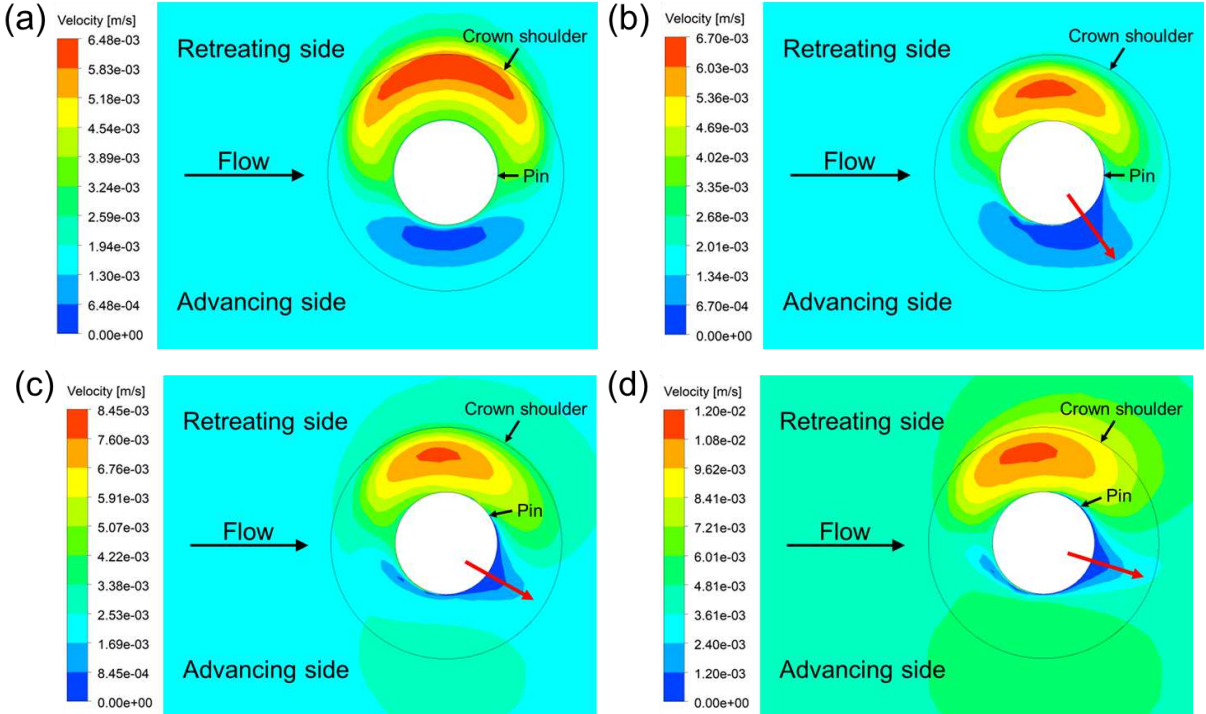


Figure 10 Velocity distribution at the mid-pin depth in (a) Case1: 100mm/min, pure velocity boundary, (b) Case2: 100mm/min, pressure-dependent velocity boundary, (c) Case3: 150mm/min, pressure-dependent velocity boundary, (d) Case4: 250mm/min, pressure-dependent velocity boundary

### 3.3 Temperature

Figure 11 shows the temperature distribution in the center of tool cross-section using pressure-dependent velocity boundary condition at the welding speed of 100mm/min. Thermal histories in the middle thickness of the workpiece are extracted at two points located at pin peripheries on both advancing and retreating sides, as illustrated in Figure 11. Figure 12 compares the corresponding thermal histories using pure velocity boundary and pressure-dependent velocity boundary under the welding speed of 100mm/min. At the pin periphery, the maximum temperature approaches the solidus of AA6061-T6 at either advancing or retreating side. With the velocity boundary condition, temperature in the advancing side is higher than that in the retreating side around the pin periphery. In contrary, with the pressure dependent velocity boundary condition, the retreating side has a higher temperature. The temperature results are closely related to the material flow behavior. With the pressure-dependent velocity boundary condition, the existence of low-pressure region limits the amount of material flow towards advancing side, as shown in the flow field in Figure 9 (b). Based on the modeling results of flow field, plasticized material is mainly deformed at the retreating side and result in a higher temperature in retreating side. With the pure velocity boundary condition, material flow is enforced in the vicinity of the pin and is transported further into the advancing side. Materials experience longer period of friction and deformation heating, which results in higher temperature at the advancing side.

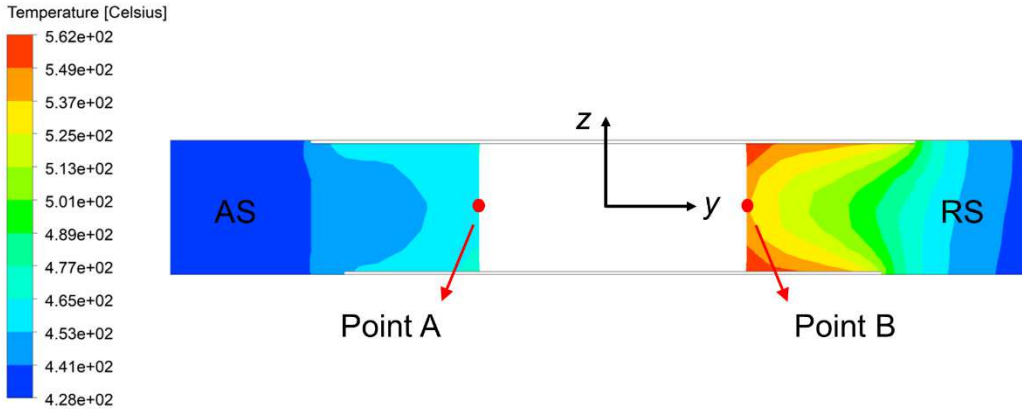


Figure 11 Positions for thermal history calculation

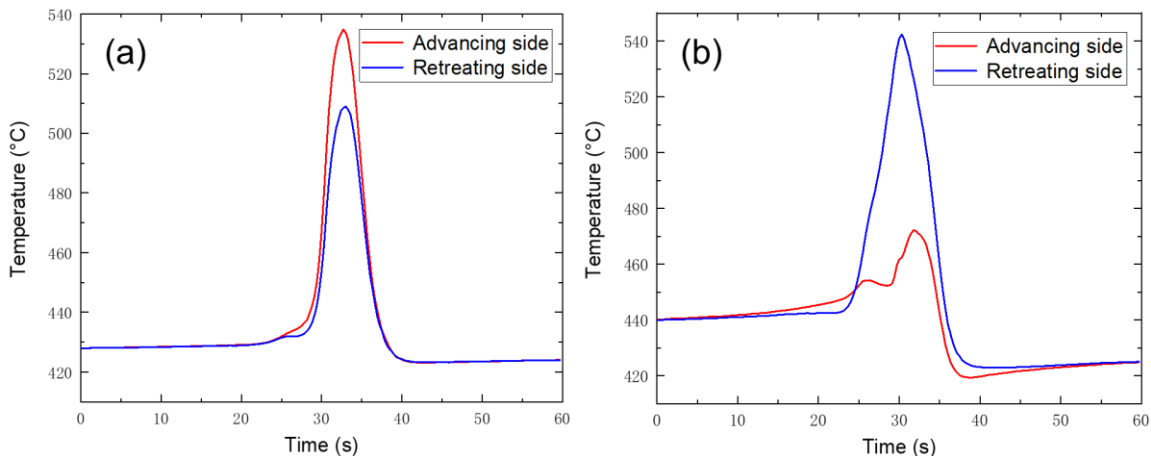


Figure 12 Thermal histories at the middle thickness of the plate on pin periphery (illustrated as point A and B in Figure 11): (a) case 1, (b) case 2

#### 4. Conclusions

In this paper, a new pressure-dependent velocity boundary condition based on Archard's wear equation is developed to model SRFSW of AA6061-T6 using CFD method. Derivation of this new T/W boundary condition is from the perspective of shear layer formation and the sticking/sliding transition state at the T/W interface is defined through the wear fraction coefficient. The main conclusions are as follows:

- The weld cross section geometry can be successfully predicted based on the strain distribution calculated from the pressure-dependent velocity boundary condition. The hourglass shape and location of the TMAZ boundary at the advancing side matches well with the experimental results.
- The pressure-dependent velocity boundary condition can robustly capture the effects of different welding speeds ranging from 100mm/min to 250mm/min on the weld geometry. The relative position of the calculated TMAZ boundary to the pin periphery at the advancing side could serve as a numerical criterion to predict void defect formation.

- Compare with pure velocity boundary condition, the pressure-dependent velocity boundary condition explicitly considers the varying pressure surrounding the pin, and leads to a more reasonable computed results of pressure and flow field distribution.

More experiments will be performed to further validate the modeling results under different welding parameters and provide accurate quantitative predictions.

## Acknowledgement

The project is supported by NASA ESI under the grant No. 80NSSC19K0216, Multiphysics Integrated Modeling of Self-Reacting Friction Stir Welding. The authors would also like to acknowledge Jeffrey W. Sowards, Fredrick Michael from NASA and Wei Zhang from The Ohio State University for discussion of the results.

## Conflict of Interest

The authors declared that they have no conflicts of interest to this work.

## Ethical Approval

The authors confirm that they have abided to the publication ethics and state that this work is original and has not been used for publication anywhere before.

## Consent to Participate

The authors are willing to participate in journal promotions and updates.

## Consent to Publish

The authors give consent to the journal regarding the publication of this work.

## Authors Contributions

Chenyu Zhao: conceptualization, methodology, investigation, validation, writing—original draft

Xun Liu: supervision, writing—review and editing

## Funding

The project is supported by NASA ESI under the grant No. 80NSSC19K0216, Multiphysics Integrated Modeling of Self-Reacting Friction Stir Welding.

## Competing Interests

The authors declare no competing interests.

## Availability of data and materials

The data supporting the conclusions are included in the article.

## References

- [1] D. Alléaux, F. Marie, Mechanical and corrosion behaviour of the 2139 aluminium-copper alloy welded by the Friction Stir Welding using the bobbin tool technique, Mater.

Sci. Forum. 519–521 (2006) 1131–1138.

- [2] R.W. Carter, Auto-adjustable tool for self-reacting and conventional friction stir welding, 2004.
- [3] H.N.B. Schmidt, T.L. Dickerson, J.H. Hattel, Material flow in butt friction stir welds in AA2024-T3, *Acta Mater.* 54 (2006) 1199–1209.
- [4] Z.W. Chen, S. Cui, Tool-workpiece interaction and shear layer flow during friction stir welding of aluminium alloys, *Trans. Nonferrous Met. Soc. China.* 17 (2007) S258–S261.
- [5] Z.W. Chen, T. Pasang, Y. Qi, Shear flow and formation of Nugget zone during friction stir welding of aluminium alloy 5083-O, *Mater. Sci. Eng. A.* 474 (2008) 312–316.
- [6] R.C. Batra, Z.G. Wei, Shear bands due to heat flux prescribed at boundaries, *Int. J. Plast.* 22 (2006) 1–15.
- [7] W. Yuan, R.S. Mishra, B. Carlson, R. Verma, R.K. Mishra, Material flow and microstructural evolution during friction stir spot welding of AZ31 magnesium alloy, *Mater. Sci. Eng. A.* 543 (2012) 200–209.
- [8] M.H. Tresca, On further applications of the flow of solids, *Proc. Inst. Mech. Eng.* 29 (1878) 301–345.
- [9] X.J. Pei, P.S. Dong, Shear localisation modelling of friction stir weld formation process, 19 (2014) 416–427.
- [10] X. Pei, P. Dong, Modeling of banded structure in friction stir weld in strain rate-hardening materials of Zener-Hollomon type, *J. Strain Anal. Eng. Des.* 50 (2015) 175–189.
- [11] Y. Zhu, G. Chen, Q. Chen, G. Zhang, Q. Shi, Simulation of material plastic flow driven by non-uniform friction force during friction stir welding and related defect prediction, *Mater. Des.* 108 (2016) 400–410.
- [12] C. Zhao, X. Liu, Computational Analysis on Weld Formation Mechanism during Self-Reacting Friction Stir Welding, *J. Manuf. Sci. Eng.* (2020) 1–15.
- [13] R. Nandan, G.G. Roy, T.J. Liernert, T. Debroy, Numerical modelling of 3D plastic flow and heat transfer during friction stir welding of stainless steel, *Sci. Technol. Weld. Join.* 11 (2006) 526–537.
- [14] X. Liu, G. Chen, J. Ni, Z. Feng, Computational Fluid Dynamics Modeling on Steady-State Friction Stir Welding of Aluminum Alloy 6061 to TRIP Steel, *J. Manuf. Sci. Eng. Trans. ASME.* 139 (2017).
- [15] A. Bastier, M.H. Maitournam, K. Dang Van, F. Roger, Steady state thermomechanical modelling of friction stir welding, *Sci. Technol. Weld. Join.* 11 (2006) 278–288.
- [16] G.Q. Chen, Q.Y. Shi, Y. Fujiya, T. Horie, Simulation of metal flow during friction stir welding based on the model of interactive force between tool and material, *J. Mater. Eng. Perform.* 23 (2014) 1321–1328.
- [17] P.A. Colegrove, H.R. Shercliff, 3-Dimensional CFD modelling of flow round a threaded

friction stir welding tool profile, *J. Mater. Process. Technol.* 169 (2005) 320–327.

- [18] H. Atharifar, D. Lin, R. Kovacevic, Numerical and experimental investigations on the loads carried by the tool during friction stir welding, *J. Mater. Eng. Perform.* 18 (2009) 339–350.
- [19] R. Nandan, G.G. Roy, T. Debroy, Numerical simulation of three dimensional heat transfer and plastic flow during friction stir welding, *Metall. Mater. Trans. A Phys. Metall. Mater. Sci.* 37 (2006) 1247–1259.
- [20] R. Nandan, G.G. Roy, T.J. Lienert, T. Debroy, Three-dimensional heat and material flow during friction stir welding of mild steel, *Acta Mater.* 55 (2007) 883–895.
- [21] R. Nandan, T. DebRoy, H.K.D.H. Bhadeshia, Recent advances in friction-stir welding - Process, weldment structure and properties, *Prog. Mater. Sci.* 53 (2008) 980–1023.
- [22] A. Arora, R. Nandan, A.P. Reynolds, T. DebRoy, Torque, power requirement and stir zone geometry in friction stir welding through modeling and experiments, *Scr. Mater.* 60 (2009) 13–16.
- [23] B.C. Liechty, B.W. Webb, Modeling the frictional boundary condition in friction stir welding, *Int. J. Mach. Tools Manuf.* 48 (2008) 1474–1485.
- [24] C.M. Sellars, W.J.M. Tegart, Hot workability, *Int. Metall. Rev.* 17 (1972) 1–24.
- [25] Klaus-Jürgen Bathe, *Finite Element Procedures*, Prentice hall, 1996.
- [26] P. Ulysse, Three-dimensional modeling of the friction stir-welding process, *Int. J. Mach. Tools Manuf.* 42 (2002) 1549–1557.
- [27] T. Sheppard, D.S. Wright, Determination of flow stress: Part 1 constitutive equation for aluminium alloys at elevated temperatures, *Met. Technol.* 6 (1979) 215–223.
- [28] H.J. Liu, J.C. Hou, H. Guo, Effect of welding speed on microstructure and mechanical properties of self-reacting friction stir welded 6061-T6 aluminum alloy, *Mater. Des.* 50 (2013) 872–878.
- [29] A.F. Hasan, C.J. Bennett, P.H. Shipway, S. Cater, J. Martin, A numerical methodology for predicting tool wear in Friction Stir Welding, *J. Mater. Process. Technol.* 241 (2017) 129–140.
- [30] J.F. Archard, Contact and rubbing of flat surfaces, *J. Appl. Phys.* 24 (1953) 981–988.
- [31] R.W. Fonda, J.F. Bingert, K.J. Colligan, Development of grain structure during friction stir welding, *Scr. Mater.* 51 (2004) 243–248.
- [32] J.C. Hou, H.J. Liu, Y.Q. Zhao, Influences of rotation speed on microstructures and mechanical properties of 6061-T6 aluminum alloy joints fabricated by self-reacting friction stir welding tool, *Int. J. Adv. Manuf. Technol.* 73 (2014) 1073–1079.
- [33] Z.W. Chen, S. Cui, On the forming mechanism of banded structures in aluminium alloy friction stir welds, *Scr. Mater.* 58 (2008) 417–420.

# Figures

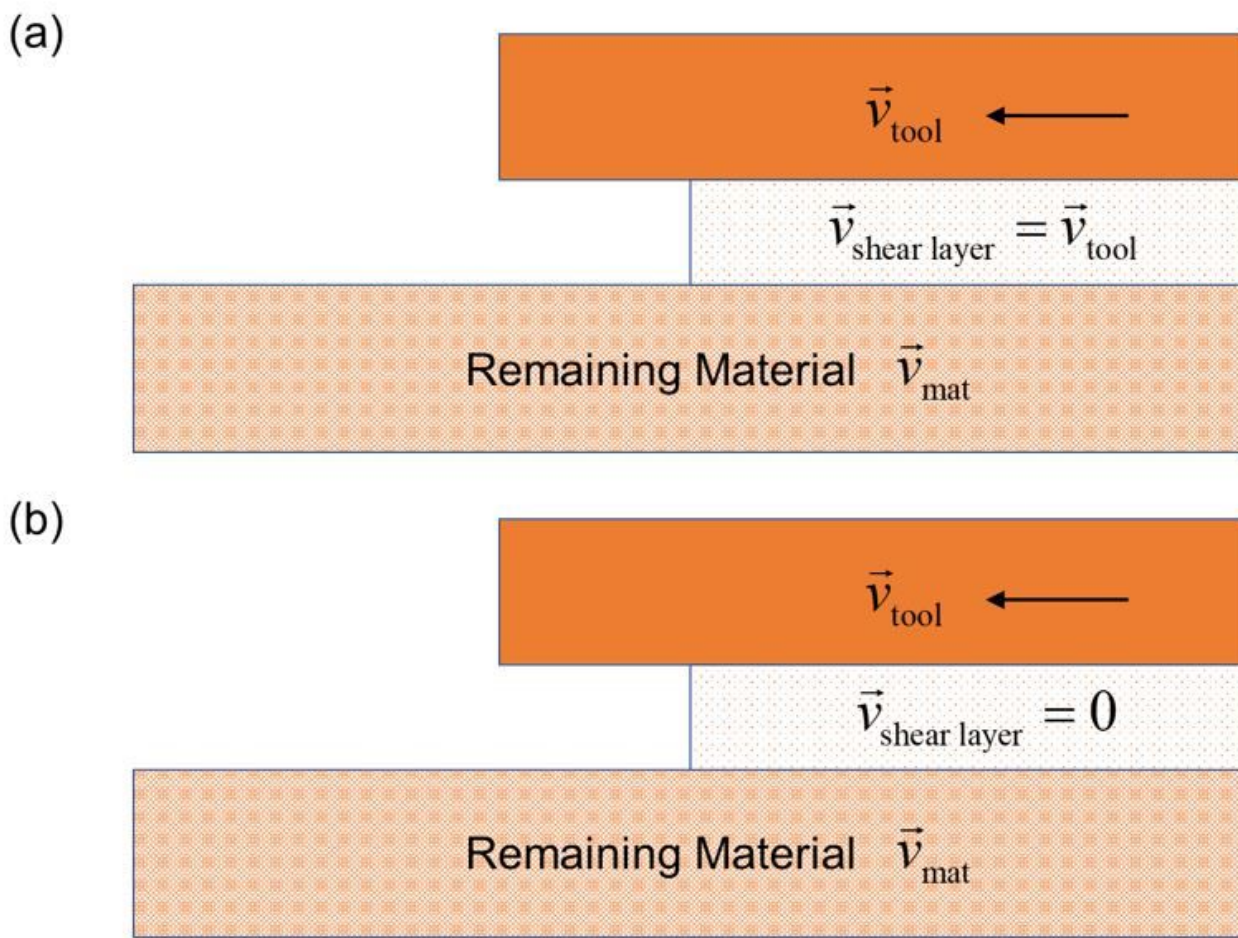
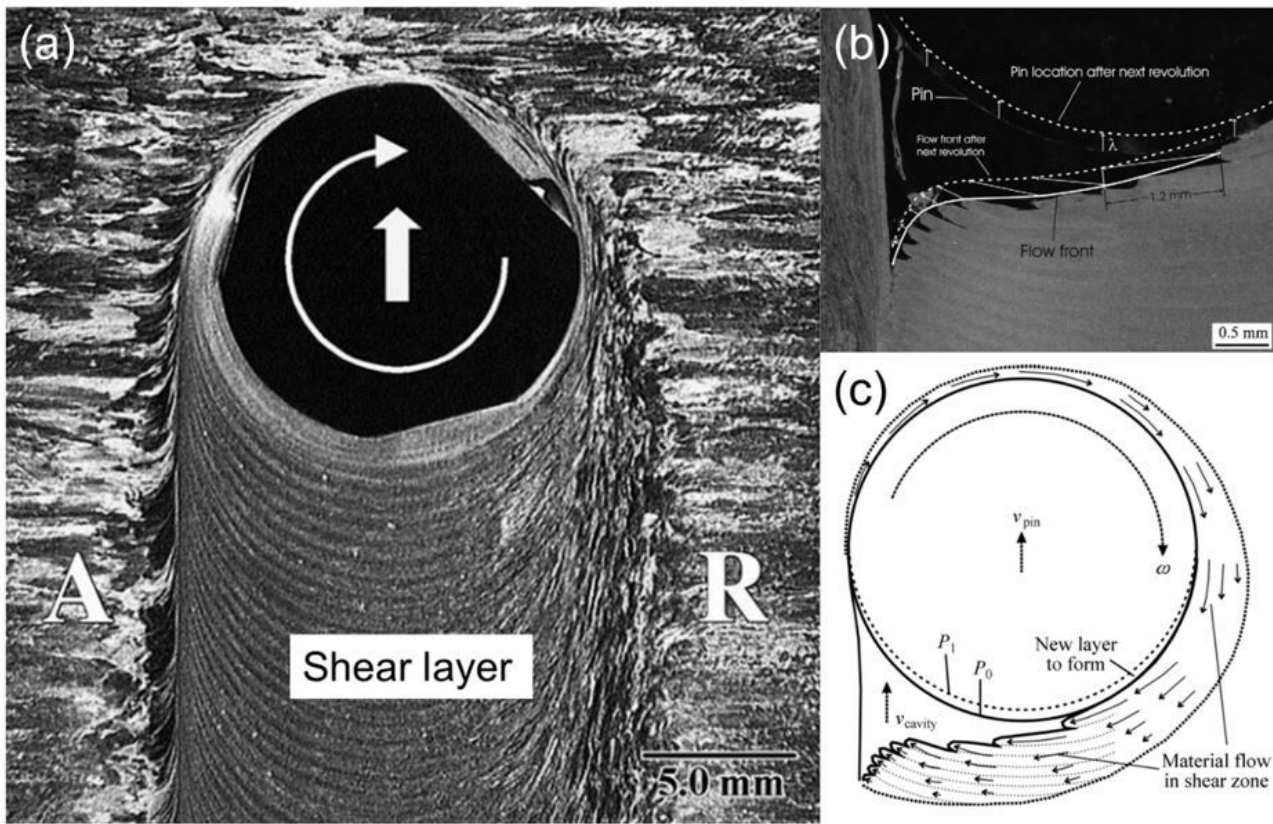


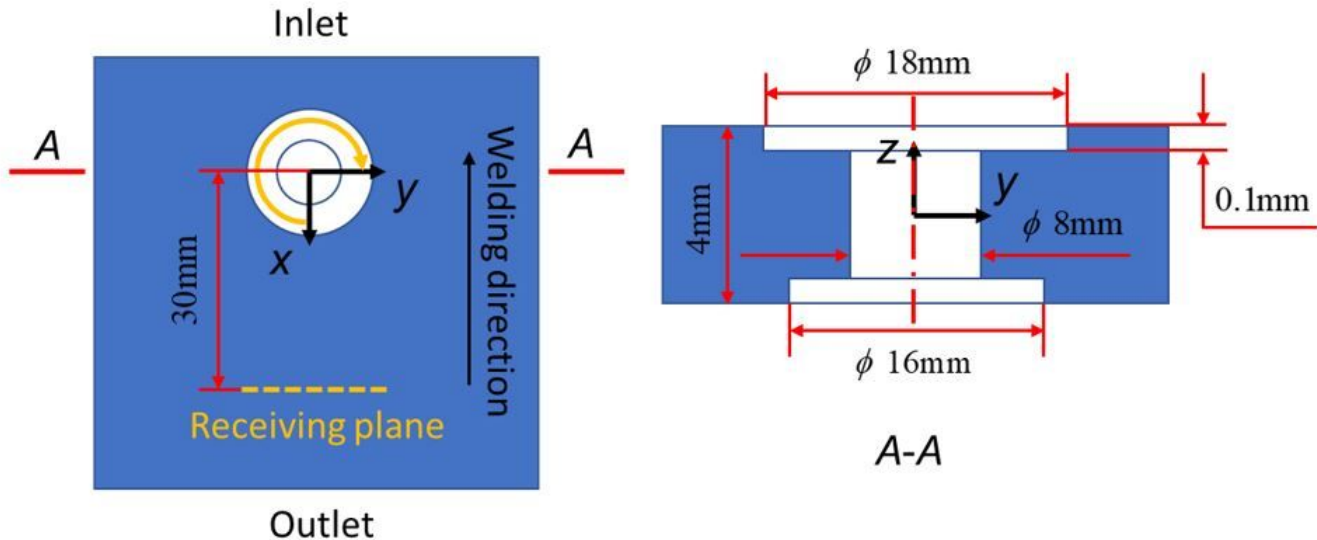
Figure 1

Illustration of sticking/sliding transition state at T/W interface: (a) Full sticking; (b) Pure sliding.



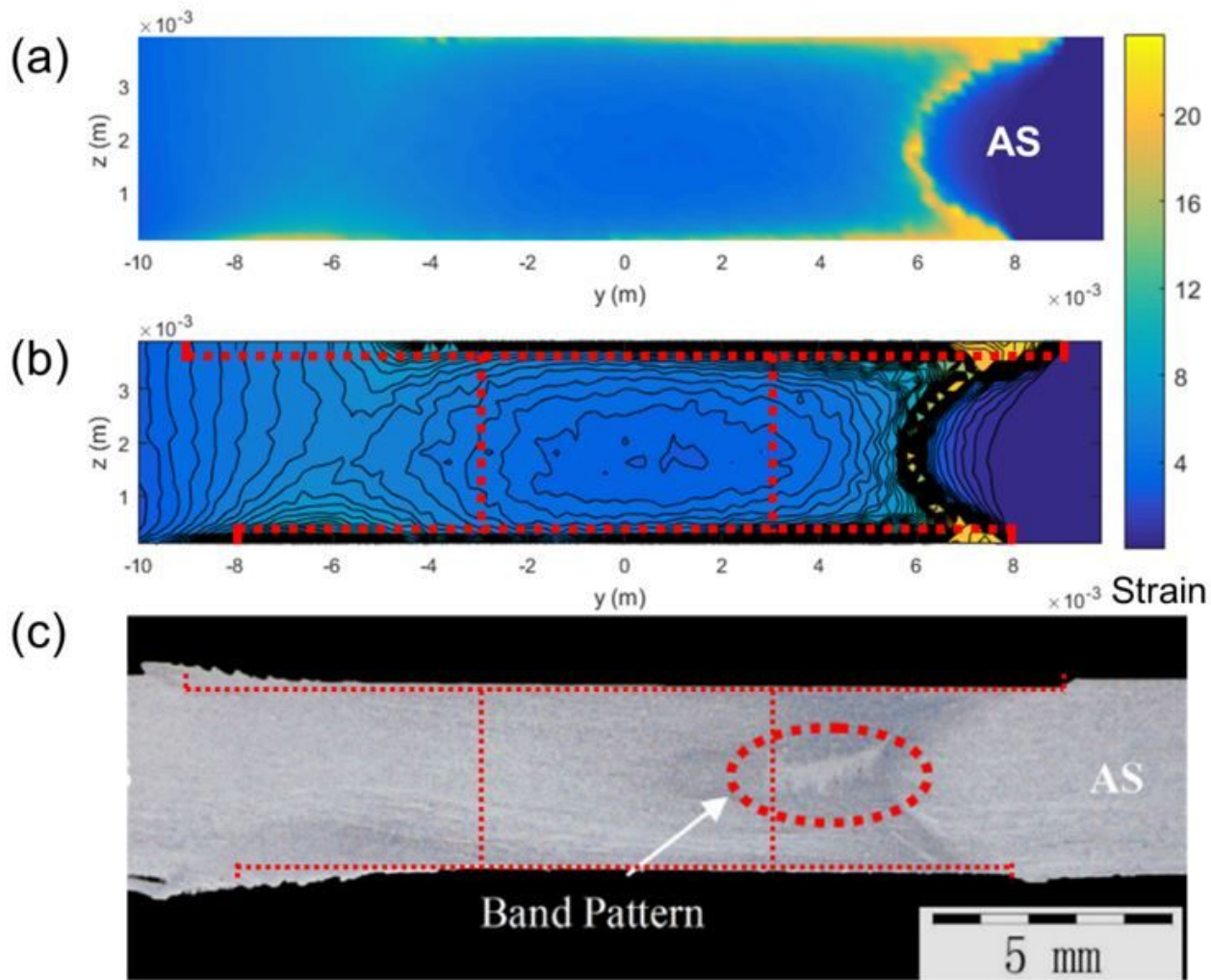
**Figure 2**

(a) Top view of shear layer in FSW [31], (b) shear layer behind the pin in FSW [5], (c) schematic illustration of shear layer around the pin [4]



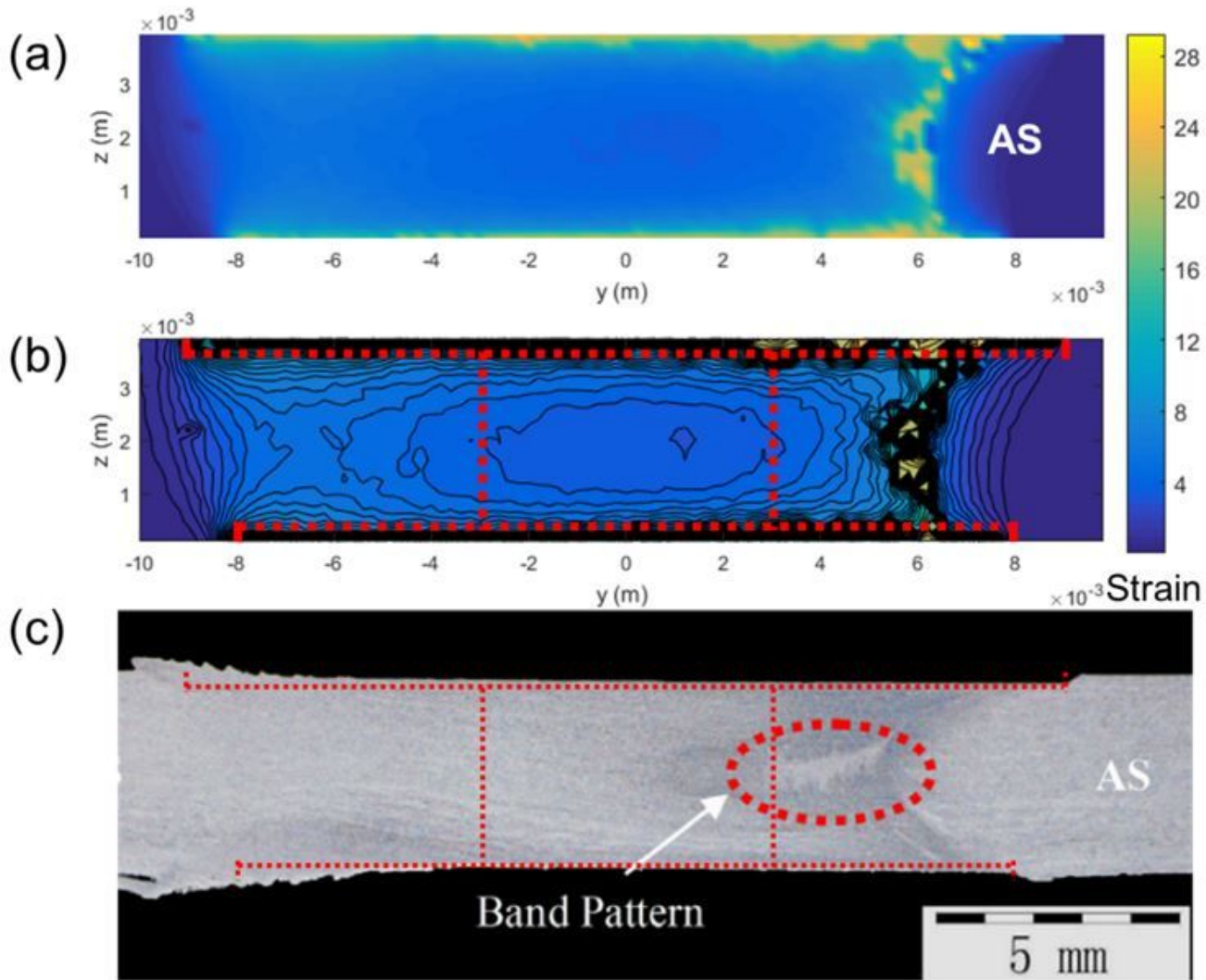
**Figure 3**

Illustration of model geometry



**Figure 4**

(a) Cloud map of predicted strain distribution at 30mm behind tool center in case 1, (b) Iso-strain contour map at 30mm behind tool center in case 1, (c) Cross section of SRFSW weld under welding speed of 100mm/min from reference [28]



**Figure 5**

(a) Cloud map of predicted strain distribution at 30mm behind tool center in case 2, (b) Iso-strain contour map at 30mm behind tool center in case 1, (c) Cross section of SRFSW weld under welding speed of 100mm/min from reference [28]

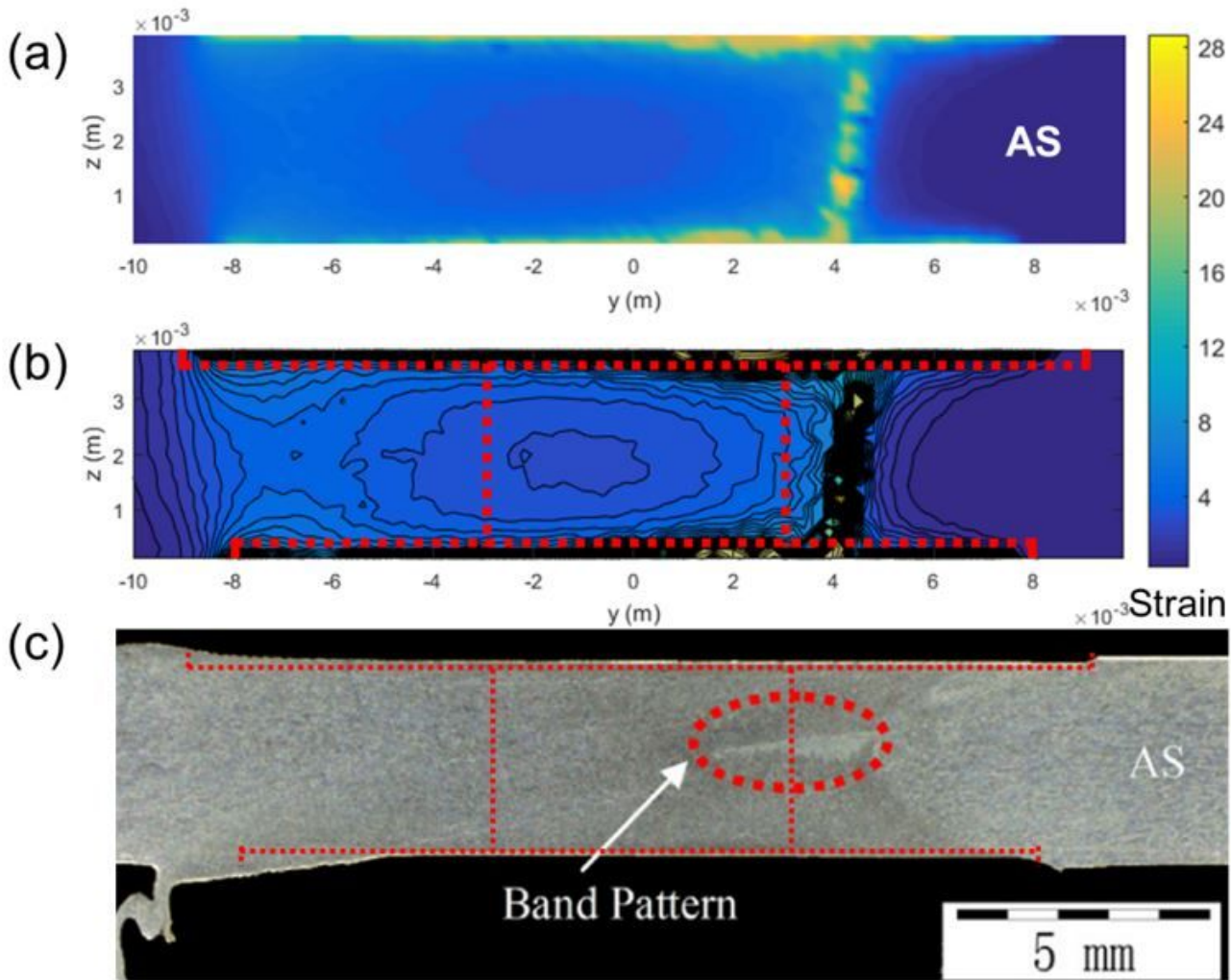


**Figure 6**

(a) Cloud map of predicted strain distribution at 30mm behind tool center in case 3, (b) Iso-strain contour map at 30mm behind tool center in case 1, (c) Cross section of SRFSW weld under welding speed of 150mm/min from reference [28]

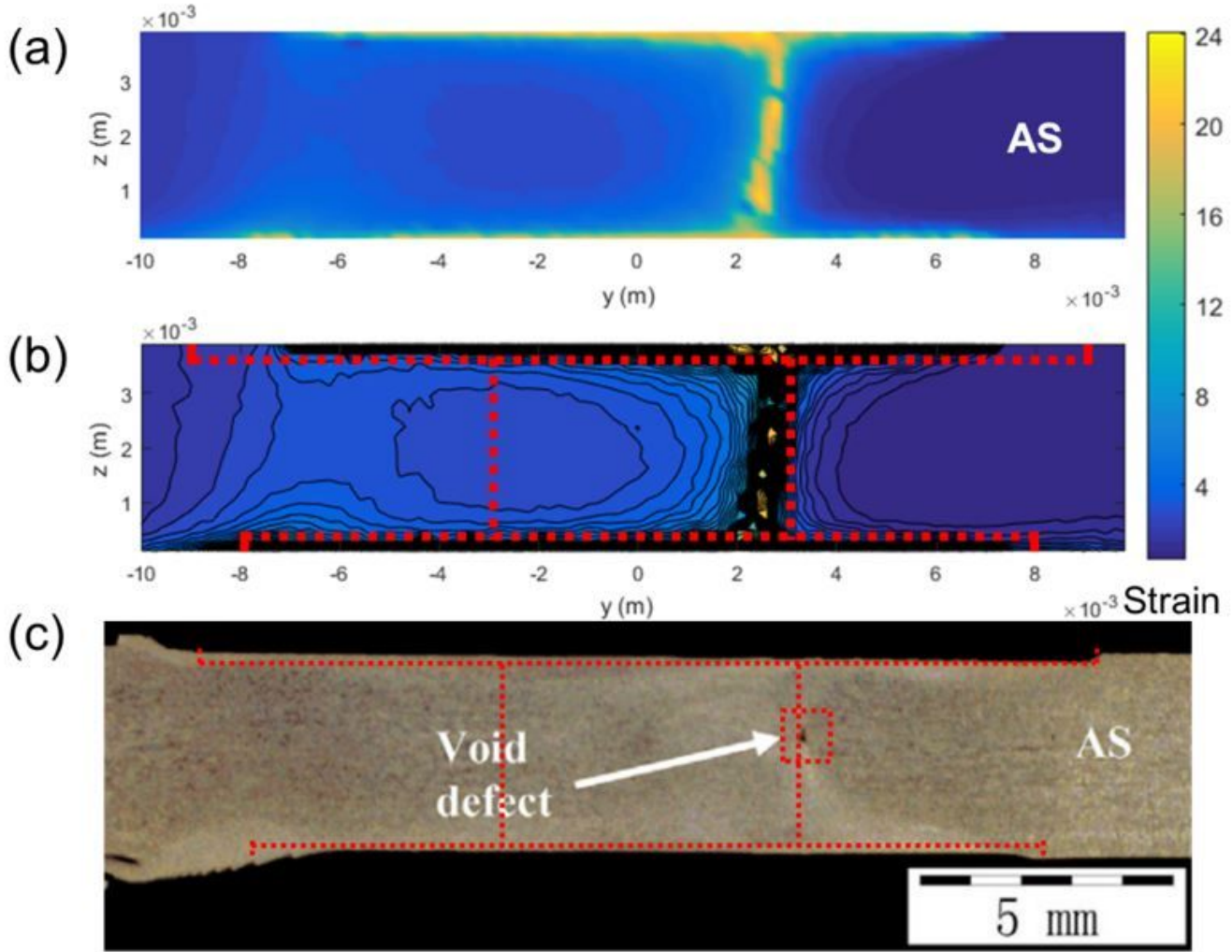


**Figure 7**

(a) Cloud map of predicted strain distribution at 30mm behind tool center in case 4, (b) Iso-strain contour map at 30mm behind tool center in case 1, (c) Cross section of SRFSW weld under welding speed of 250mm/min from reference [28]

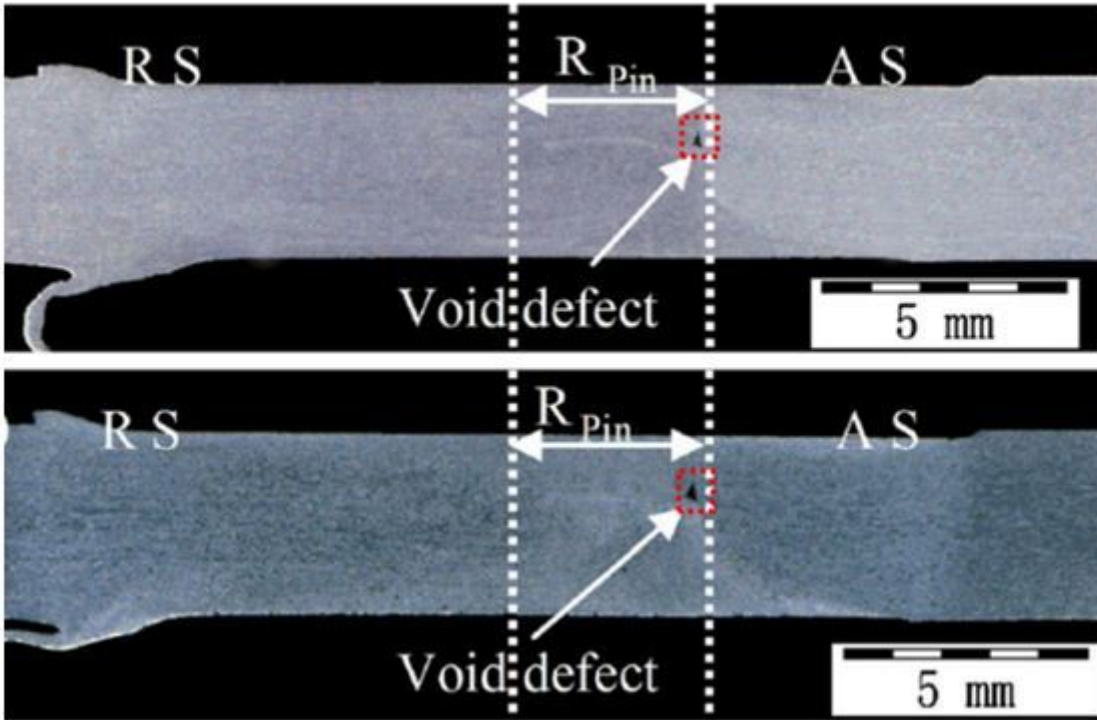


**Figure 8**

Cross section of SRFSW welds of AA6061-T6 from reference [32]

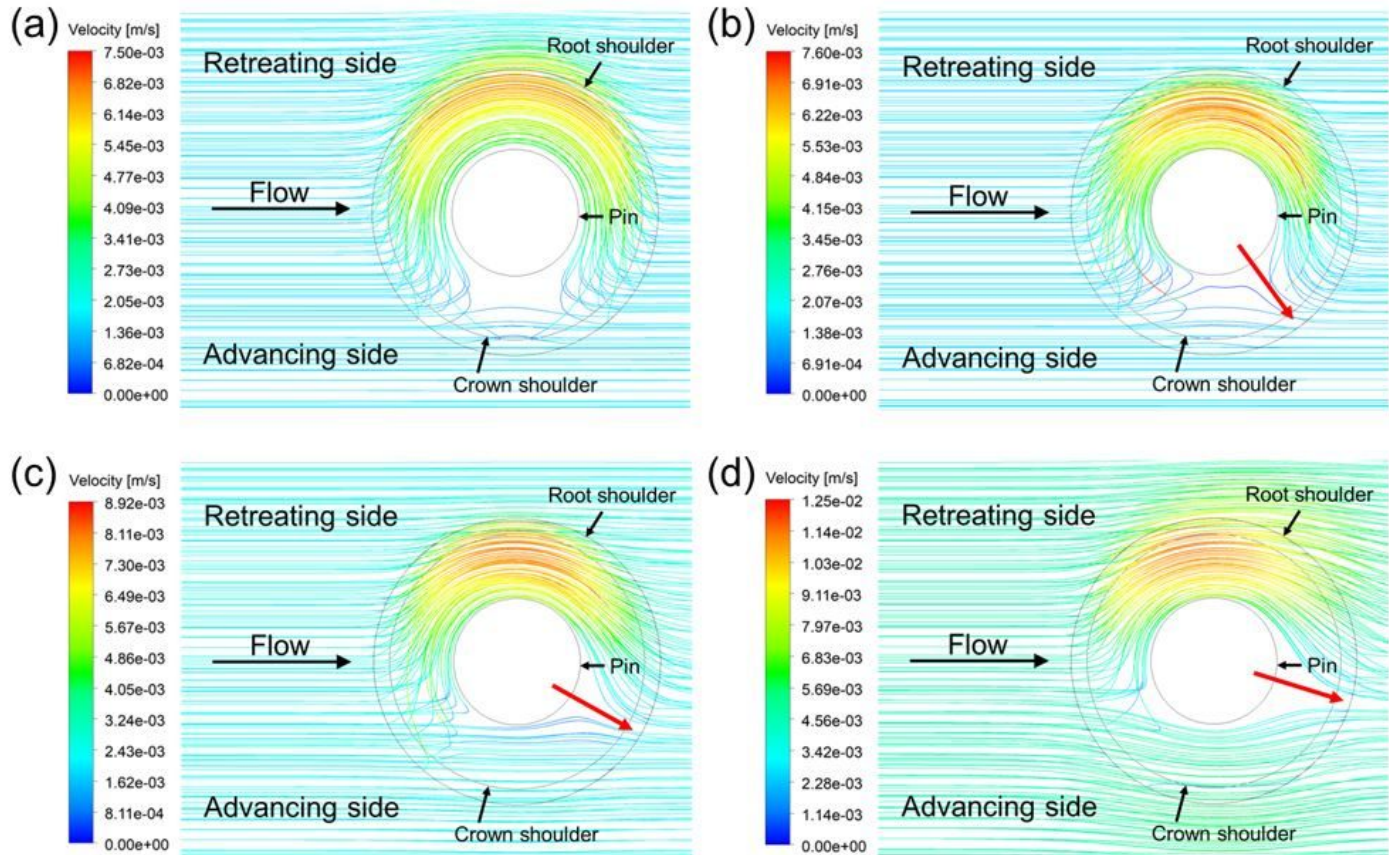


**Figure 9**

Material flow field in (a) Case1: 100mm/min, pure velocity boundary, (b) Case2: 100mm/min, pressure-dependent velocity boundary, (c) Case3: 150mm/min, pressure-dependent velocity boundary, (d) Case4: 250mm/min, pressure-dependent velocity boundary

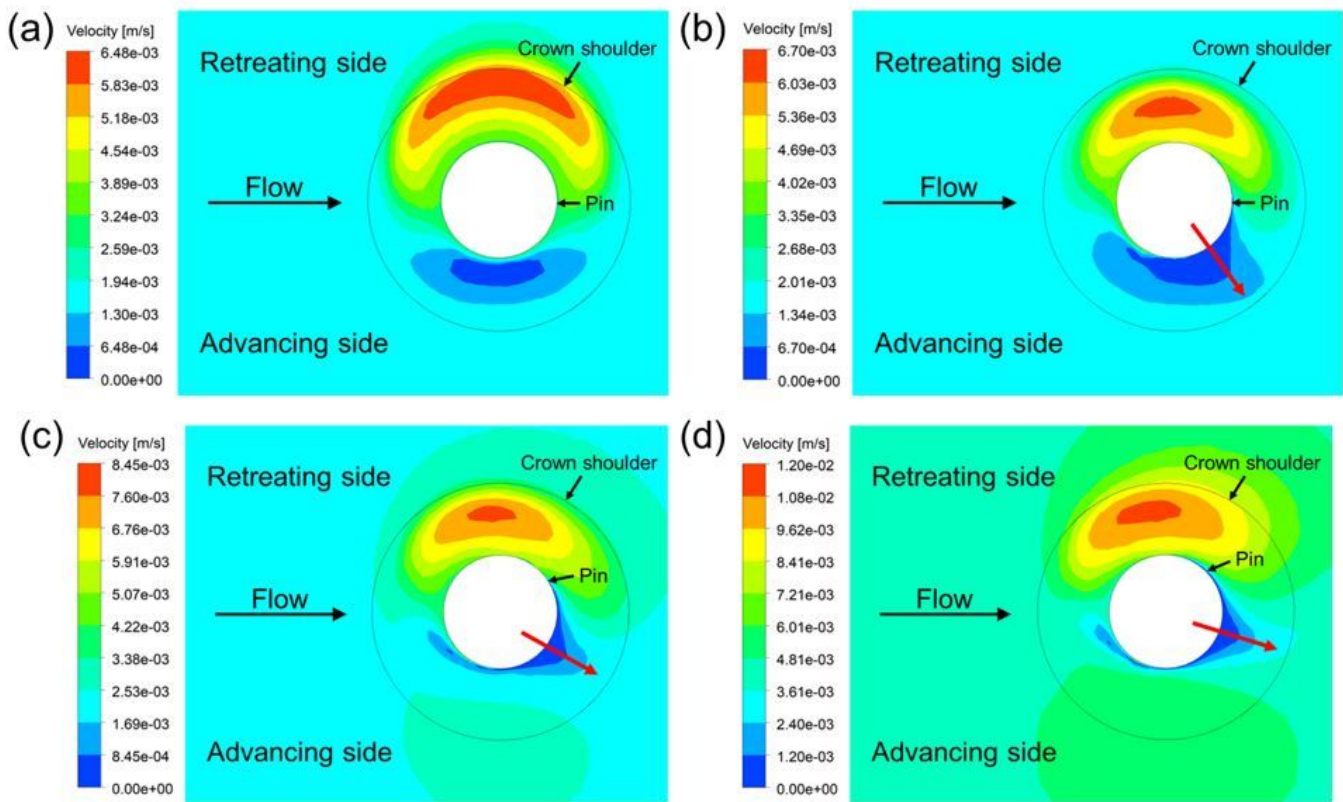


**Figure 10**

Velocity distribution at the mid-pin depth in (a) Case1: 100mm/min, pure velocity boundary, (b) Case2: 100mm/min, pressure-dependent velocity boundary, (c) Case3: 150mm/min, pressure-dependent velocity boundary, (d) Case4: 250mm/min, pressure-dependent velocity boundary

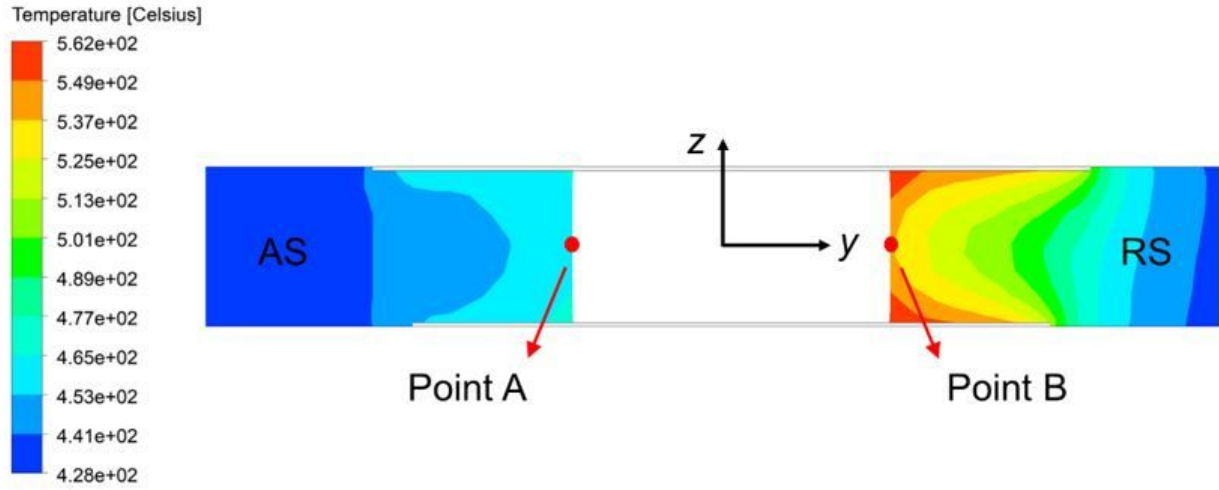


**Figure 11**

Positions for thermal history calculation

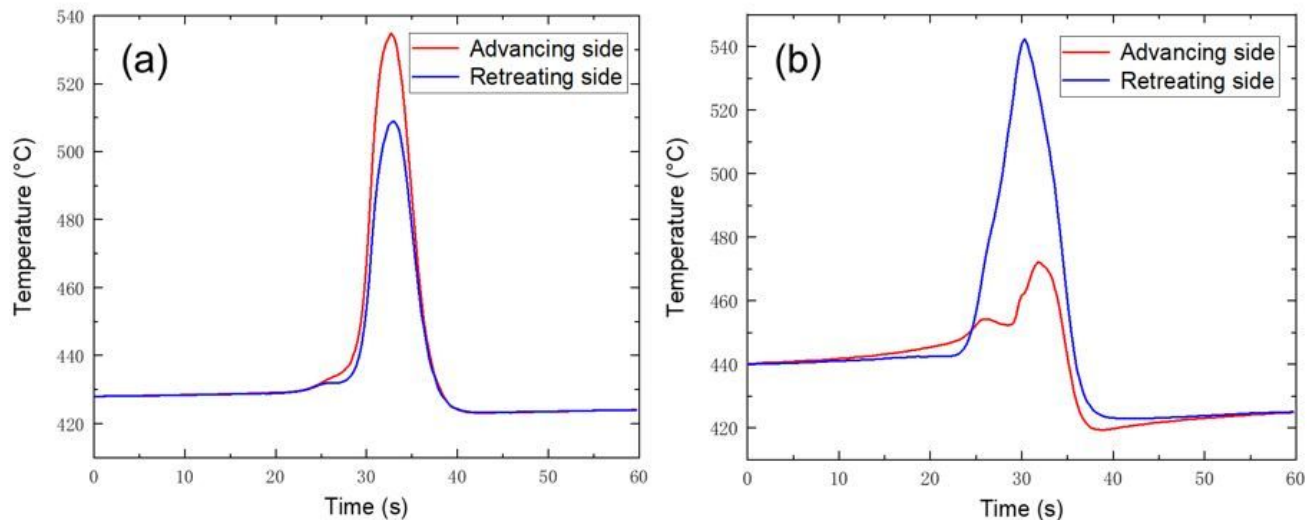


**Figure 12**

Thermal histories at the middle thickness of the plate on pin periphery (illustrated as point A and B in Figure 11): (a) case 1, (b) case 2